FT-IR spectroscopy study of HNCO adsorption and hydrolysis over oxide-based samples dedicated to deNO x processes

M. Barreau, Xavier Courtois, F. Can

Applied Catalysis A: General 552 (2018) 147-153
DOI: 10.1016/j.apcata.2017.12.019

FT-IR spectroscopy study of HNCO adsorption and hydrolysis over oxide-based samples dedicated to deNO$_x$ processes.

M. Barreau, X. Courtois* and F. Can*

University of Poitiers, CNRS, UMR 7285
Institut de Chimie des Milieux et Matériaux de Poitiers (IC2MP)
4 rue Michel Brunet – TSA 51106 – 86073 Cedex 9, France
Fax: (+) +33 5 49 45 37 41
E-mail: xavier.courtois@univ-poitiers.fr; fabien.can@univ-poitiers.fr

Abstract: HNCO adsorption monitored by FT-IR spectroscopy was performed over a wide range of oxides from various acid-base and redox properties: SiO_2, Al_2O_3, TiO_2, ZrO_2, CeO_2, CeO_2-ZrO_2, WO_3/CeO_2-ZrO_2. HNCO adsorbed dissociatively in the whole studied samples. A correlation with pyridine ν_{8a} wavenumbers revealed that HNCO dissociation mainly involved weak Lewis acid sites (LAS) location. The significant isocyanate adsorption capacity of titania and zirconia was evidenced. HNCO hydrolysis reaction was also investigated. Among the various studied samples, CeO_2-ZrO_2 and WO_3/CeO_2-ZrO_2 presented the higher HNCO hydrolysis rate, with ammonia formation from room temperature. For all studied samples, –NCO groups were evidenced as intermediate species of HNCO hydrolysis.

Keywords: Isocyanic acid; HNCO hydrolysis; Infrared spectroscopy; oxide-based catalysts; DeNO$_x$.

1. Introduction

NO_x emissions control from lean-burn engines remains an important challenge for the academic and industrial communities. Among the various processes available to perform NOx (NO and NO_2) abatement, the NO_x storage reduction (NSR) and the selective catalytic reduction (SCR) processes are viable solutions to control NO_x emission in excess of oxygen. Interestingly, whatever the considered reductants, both technologies involve mechanisms implying the formation of reactive species like –CN and –NCO, possibly leading to ammonia formation, as key intermediates in the N_2 formation. For instance, such species were identified during the lean NO_x reduction by propene over various materials such as perovskites [i], supported transition metals [ii], or supported noble catalysts [iii]. Use of alkanes like propane [iv] or decane [v] also led to NH_3 intermediate species over Cu-ZSM-5 exchanged zeolite, as well as during the NO_x reduction process by ethanol over Ag/Al_2O_3 catalyst [vi]. In fact, the direct use of ammonia as reductant is one of the most efficient process to reduce NO_x from gaseous mixtures containing an excess of oxygen, initially developed for stationary sources. Nevertheless, on boarded ammonia is not suitable (highly toxic and corrosive) and the automotive industry has commonly adopted the safer Urea-SCR technology. Urea (NH_2-CO-NH_2) is theoretically decomposed in ammonia via two consecutives reactions: the "urea thermolysis" (Eq. 1) leading to NH_3 and HNCO, and the "HNCO hydrolysis" (Eq. 2), leading to the second NH_3 molecule.

$$(NH_2)CO(NH_2) \rightarrow NH_3 + HNCO \quad (1)$$

$$HNCO + H_2O \rightarrow NH_3 + CO_2 \quad (2)$$

The HNCO hydrolysis reaction was previously studied in the literature to ensure the desired production of ammonia [vii].Recently, the competitive reactivity of the HNCO intermediate species with NO_x was also evidenced during urea-SCR process [viii]. In addition to the desired hydrolysis reaction, it has been showed that HNCO also competes with O_2 and NO_x. During the SCR process, a mix of both NO and NO_2 was evidenced to react with HNCO and contribute to the NO_x reduction, resulting in another deNO_x pathway [viii].

Finally, mechanistic studies agree that isocyanate species (–NCO) are highly reactive intermediates toward NO+O_2 and/or surface nitrite or nitrate species to produce N_2. Consequently, the study of HNCO and –NCO interactions with surface of catalysts appears essential to highlight the deNO_x chemistry. Obviously, despite a major interest due to its importance as an intermediate in virtually all the deNO_x reactions, its surface reactivity is poorly documented. Indeed, HNCO is not available as commercial product and only few means are reported to produce pure gaseous HNCO. In this work, gaseous isocyanic acid was obtained from the decomposition of cyanuric acid, based on the work published by Perry *et al.* [ix]. The present work is a first step in a deeper characterization of competitive reactions of gaseous HNCO and isocyanates species with the exhaust gas components like NO_x. Consequently, the

HNCO adsorption and hydrolysis reaction was firstly studied by infrared spectroscopy over various oxides selected for their different acid-base and redox properties (SiO_2, Al_2O_3, TiO_2, CeO_2, ZrO_2, CeO_2-ZrO_2 and supported WO_3/CeO_2-ZrO_2).

2. Material and methods

Materials used in this study are listed in Table 1. Silica was used as model material for FTIR characterization, alumina as model heterogeneous oxide support, titania and zirconia as model catalysts for urea thermolysis and HNCO hydrolysis, respectively, ceria and ceria-zirconia (40_{wt}% of CeO_2, thereafter denoted Ce-Zr) as model redox oxides and finally WO_3/Ce-Zr as model supported SCR catalyst [x-xii]. All oxides were provided by chemical companies as reported in Table 1, except for supported WO_3 catalyst. For this sample, Ce-Zr support (provided by Solvay) was first calcined 4 hours under air at 700°C. Tungsten (6_{wt}% WO_3) was added by wet impregnation at 60°C under continuous agitation using an aqueous solution of ammonium metatungstate. After drying at 80°C, the preparation was placed in an oven at 120°C during a night. Finally all samples were calcined in wet air 4 hours at 700°C (heating rate: 5° min^{-1}).

Specific surface areas were determined by nitrogen adsorption at 77 K using the BET method (Tristar 3000, Micromeritics). Prior to the N_2 physisorption, the samples were degassed under vacuum 2 h at 250°C.

Catalysts were characterized by powder X-ray diffraction using a Bruker D5005 diffractometer equipped with a monochromatized Cu K_α radiation (λ = 1.5418 Å) operated at 40 kV and 30 mA. The diffraction patterns were recorded in the 15-75° 2θ value range, with a step of 0.04 ° sec^{-1} and a step time of 6 s. Crystalline phases were identified by comparison with ICDD database files.

Table 1. Physical properties of the studied samples.

samples	provider	B.E.T surface area (m^2 g^{-1})	XRD [ICDD]
SiO_2	Aerosil 90, Degussa	38	
Al_2O_3	GOD 215, Axens	176	00-050-0741(I)
TiO_2	Aldrich	13	96% rutile 00-034-0180 4% anatase 21-1272
CeO_2	HAS 1A, Solvay	43	34-0394
ZrO_2	Solvay	16	79-1766
CeO_2-ZrO_2 (Ce-Zr)	Solvay	73	38-1436
WO_3/Ce-Zr	Wet impregnation of $(NH_4)_{10}W_{12}O_{41}\cdot 5H_2O$ salt, Alfa Aesar	52	38-1436

The surface acidity of materials was evaluated by pyridine adsorption monitored by IR spectroscopy. IR spectra were collected with a Nexus Nicolet spectrometer equipped with a DTGS detector (Deuterium TriGlyceride Sulfur) and a KBr beam splitter. IR spectra were recorded with a resolution of 4 cm^{-1} and 64 scans. The presented spectra were normalized to a disc of 10 mg/cm^2. After sample activation at 400 °C (residual pressure of about 5.10^{-5} hPa), pyridine was adsorbed (200 Pa at equilibrium) at room temperature (RT). Desorption was performed up to 400 °C, by temperature step of 50 °C under dynamic vacuum.

Interaction of HNCO with oxide solids was studied by transmission mode infrared spectroscopy using a home-made dynamic cell, presented in Fig. 1. The sample holder is associated with a screw which allow to move away the wafer from the infrared beam to record gas phase spectra, while the sample remains in heated zone of the oven. Consequently, the design of this specific IR cell enables to collect IR spectrum of adsorbed species and gaseous compounds at the same temperature (25-400 °C). IR spectra were recorded on a Nicolet 6700 spectrometer equipped with a MCT detector and a KBr beamsplitter using a resolution of 4 cm^{-1} and 64 scans. Samples were pressed as self-supported wafer (disc of about 20 mg, 2 cm^2) and were firstly treated *in situ* in the cell at 400 °C under dynamic vacuum (residual pressure of about 5.10^{-5} hPa).

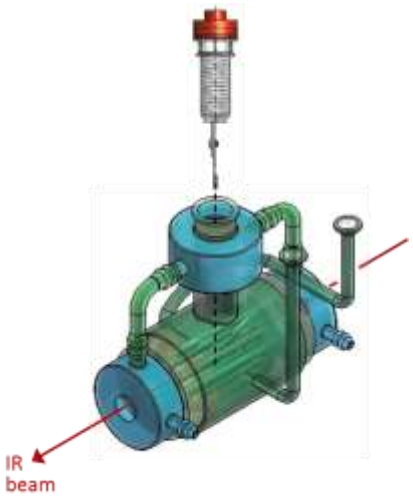

Figure 1. Design of the home-made IR cell for high temperature *in situ* adsorption of probe molecule.

Isocyanic acid was produced by depolymerising the cyclic trimer of cyanuric acid (provided by Alfa Aesar, 99 % purity) after heated at 340°C, in accordance with Eq. 3 [ix].

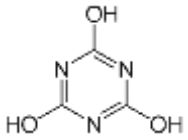

$\xrightarrow{\Delta}$ 3 O=C=NH (3)

Cyanuric acid, a nontoxic triazine white powder, was placed on a round-bottom flask with a located controlled heated zone connected to the vacuum manifold system of FT-IR experiments. After heated at 340 °C, the equilibrium HNCO pressure was about 10 hPa. Pure isocyanic acid was then expanded in the cell via calibrated doses at RT up to equilibrium by addition of accurately known increments. First, experiments were performed without oxide, in order to ensure a calibration by integrating gaseous HNCO bands. Then, HNCO adsorption was investigated over the studied oxide. At equilibrium (10 hPa), a spectrum of the gas phase was recorded, allowing to determine the amount of HNCO not adsorbed by the oxide tested. By subtracting the remaining amount to the initial amount of HNCO, an absorption capacity of each oxide can be deduced at RT.

A second set of experiments were performed with similar procedure but with water co-adsorption in order to highlight HNCO hydrolysis rate over the studied oxides. In this case, cyanuric acid was heated until the equilibrium HNCO pressure reach 5 hPa. Water was then added, by another round-bottom flask, in order to reach a total pressure of 10 hPa, corresponding to a HNCO/H_2O ratio of 1. IR spectra of adsorbed species and gas phase were then recorded from RT up to 400 °C, by 25 °C step.

Presented spectra were normalized to a disc of 10 mg cm^{-2} and the reference spectra (recorded after calcination at RT) were systematically subtracted to highlight the adsorbed species.

3. Results and discussion

3.1 XRD characterisation

The XRD patterns (supplementary material, Fig. S1) of selected oxides were consistent with the literature. Alumina material displayed the classical γ-Al_2O_3 structure [ICDD PDF n° 00-050-0741(I)]. TiO_2 mainly indicated rutile crystal phase (2θ = 27.4, 36.1 and 54.3°) with a low content (4%) of anatase mixture (2θ = 25.4, 37.9 and 48.1°). Pure CeO_2 sample calcined at 700 °C was composed of cubic CeO_2 with fluorite structure with diffraction peaks at 2θ = 28.8, 47.7 and 56.5°. The addition of zirconia to ceria led to a shift of XRD peaks to higher values, and to the appearance characteristic peaks of monoclinic zirconia, at 2θ = 30.3, 50.5 and 44.8°. Consequently, the Ce-Zr (40-60) solid showed a broad band which was observed at 2θ=29.1° between pure c-CeO_2 (28.4°, JCPDS 34-0394) and pure t-ZrO_2 (30.2°, JCPDS 79-1766), which was attributed to $Ce_{0.5}Zr_{0.5}O_2$ solid solution due to the replacement of Ce^{4+} ions (0.97 Å) by the smaller Zr^{4+} ions (0.84 Å). After WO_3 impregnation over Ce-Zr, no modification

of XRD patterns was observed, with no peaks associated to tungsten species, suggesting a good dispersion of tungsten trioxide phase as previously reported [xii].

3.2 Surface acidity characterisation

The surface acidity was determined by IR spectroscopy of adsorbed pyridine, which is one of the most largely used basic probe molecules for surface acidity characterization. Due to the nitrogen electron lone pair, pyridine interacts with acidic centers in a specific way to form (i) the pyridinium ion on protonic sites (PyH^+) and (ii) coordinated species on Lewis acid sites (PyL), giving rise to ν_{8a}, ν_{8b}, ν_{19a} and ν_{19b} ring vibration modes. Pyridine (200 Pa at equilibrium) was adsorbed at room temperature, and then desorbed by temperature steps of 50°C up to 450°C, as previously mentioned in the experimental part. Fig. 2 presents the IR spectra of the samples after pyridine evacuation at 100°C.

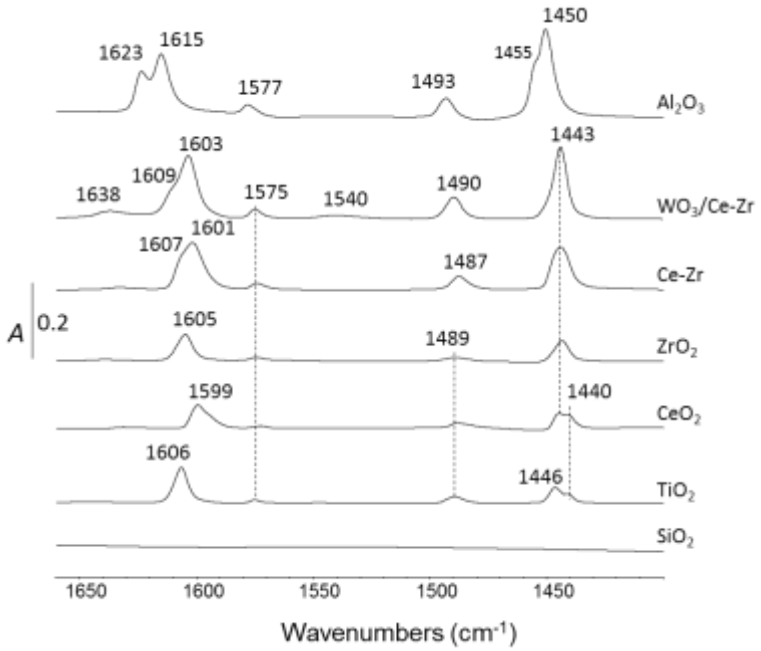

Figure 2. IR spectra of pyridine evacuated at 100°C on SiO_2, TiO_2, CeO_2, ZrO_2, (WO_3)Ce-Zr and Al_2O_3 samples. Spectra are normalized to a disc of 10 mg cm^{-2}.

As expected, the spectrum of SiO_2 displays no peak. In most samples, only pyridine coordinated on Lewis acid sites (LAS) is observed. Only WO_3/Ce-Zr catalyst exhibited characteristic frequencies of pyridinium surface species by ν_{8a}-absorption at 1638 cm^{-1} in association to ν_{19b}-absorption mode at 1540 cm^{-1} from very weak intensities. These results are in accordance with the literature [xii,xiii] which reported the IR spectra of pyridine adsorbed on tungstated zirconia and $Ce_xZr_{1-x}O_2$ mixed-oxide supported WO_3 catalysts. In Fig. 2, bands assignable to ν_{19b} and ν_{8a} mode of coordinatively bound pyridine are observed for Al_2O_3 (1450-1455 and 1615-1623 cm^{-1}), WO_3/Ce-Zr (1443 and 1603-1609 cm^{-1}), Ce-Zr (1443 and 1601-1607 cm^{-1}), ZrO_2 (1443 and 1605 cm^{-1}), CeO_2 (1440-1443 and 1599 cm^{-1}) and TiO_2 (1440-1446 and 1606 cm^{-1}), which are consistent with the literature [xiv-xvii]. Bands at 1575-1577

cm^{-1} and 1487-1493 cm^{-1} are assigned to ν_{8b} and ν_{19a} ring vibration (ν_{CCN} stretch), respectively. The higher ν_{8a} frequencies are attributed to strong LAS and correspond to 1623, 1609 and 1607 cm^{-1} for Al_2O_3, WO_3/Ce-Zr and Ce-Zr, respectively. Consequently, the lower ν_{8a} wavenumbers at 1615, 1606, 1605, 1603, 1601 and 1599 cm^{-1} are assigned to weak LAS and correspond to Al_2O_3, TiO_2, ZrO_2, WO_3/Ce-Zr, Ce-Zr and CeO_2, respectively. These attributions are used subsequently to highlight isocyanate adsorption sites (section 3.6).

The ν_{19b} mode (1440-1455 cm^{-1}) allows the quantification of the total amount of coordinated pyridine, obtained from the surface area of the corresponding absorption band using its molar coefficient. Tamura *et al*. verified that the integrated molar extinction coefficients for Lewis acidic metal oxides do not markedly depend on the nature of oxides [xiv]. This indicates that the averaged extinction coefficient for pyridine adsorption on Lewis acid sites (1.73 cm μmol^{-1}) can be used to quantify the LAS concentrations of the whole materials. Consequently, LAS concentration (expressed in $\mu mol\ g^{-1}$) is reported in Table 3 for pyridine evacuated at RT and 100°C (supplementary material, Fig. S2). For pyridine evacuated at RT, alumina and ceria-zirconia oxides presented the higher LAS concentration, with around 115 and 71 $\mu mol\ g^{-1}$. However, when pyridine was evacuated at higher temperature (100°C), WO_3/Ce-Zr sample exhibited higher acidic sites concentration than Ce-Zr host support. It indicates that deposition of WO_3 over ceria-zirconia increased the amount of stronger Lewis acid sites. Due to the variation of specific surface area of various samples, the LAS density (expressed in $\mu mol\ m^{-2}$) is reported versus the pyridine temperature evacuation in Fig. 3. From this Figure, the amount and the strength of LAS can be discussed for the whole oxides. It appears that TiO_2 and ZrO_2 presented the largest density of acid sites, but it rapidly dropped for higher pyridine temperature evacuation. These oxides also presented the lower specific surface area (Table 1). To the opposite, WO_3/Ce-Zr and Al_2O_3 oxides presented LAS with higher strength, because the declines of adsorbed pyridine with temperature were less pronounced.

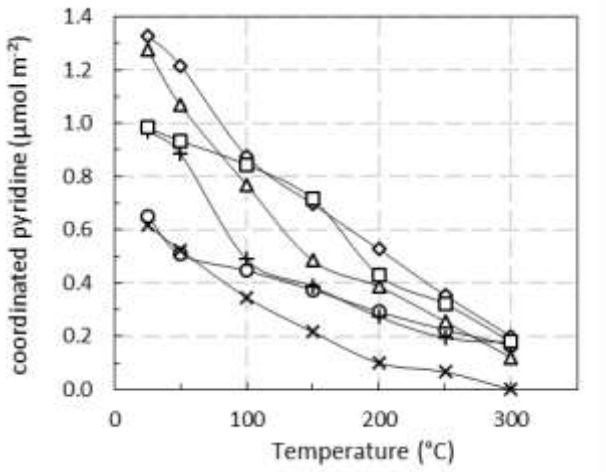

Figure 3. Lewis acid sites concentration ($\mu mol\ m^{-2}$) of the metal oxides. (○): Al_2O_3; (□): WO_3/Ce-Zr; (×): CeO_2; (+): Ce-Zr; (◇): TiO_2; (△): ZrO_2.

3.3 Gaseous isocyanic acid spectrum and calibration

IR spectra of gaseous HNCO at various equilibrium pressures are presented in Fig. 4 in the 5000-800 cm^{-1} spectral range. No other compounds than HNCO was observed, illustrating the validity of the $(HNCO)_3$ decomposition (eq. 3) to yield pure gaseous isocyanic acid. The IR frequencies assignment are reported in Table 2 and are consistent with the works of Lowenthal et *al.* [xviii] and Teles et *al.* [xix]. The six vibrational modes of the molecule correspond to three in plane stretches, two in plane bends and one out of plane bend. In the 4500-1000 cm^{-1} region, only the stretching mode was observable. The three highest energy vibrations are assigned to ν_1 (N-H stretching), ν_2 (antisymmetric NCO stretching) and ν_3 (symmetric NCO stretching) modes. The ν_3 mode being weakly intense, this band may be also assigned to Fermi resonance split components involving $\nu_4 + \nu_5$ (1353 cm^{-1}, Table2).

The integration of IR bands reported in Fig. 4 enables to calibrate the various vibrational modes of gaseous HNCO. Supplementary experiments using addition of accurately known increments were also performed. The intensity of ν_2 bands are plotted in Fig. 5 versus the amount of added isocyanic acid (○: µmol) and the equilibrium pressure of gaseous HNCO (△: Pa). The straight line indicates a correlation which will be used subsequently to determine the maximum amount of HNCO adsorbed for all the studied oxides, based on the residual pressure of isocyanic acid after adsorption on such materials (section 3.6). An experimental error within 15 % is denoted.

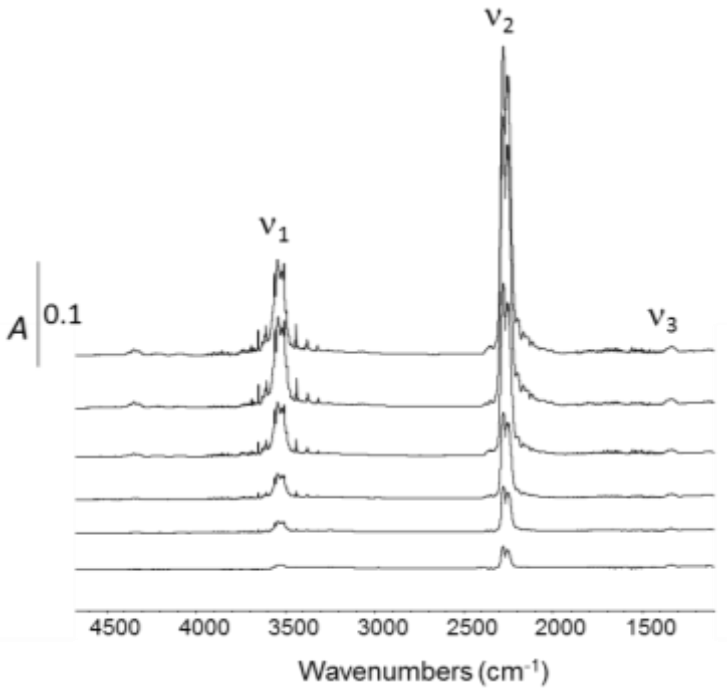

Figure 4. IR spectra of gaseous HNCO at various equilibrium pressures (from 50 to 400 Pa).

Table 2. IR vibrational assignment of gaseous HNCO [18,19].

Mode	Assignment	Frequency (cm^{-1})
ν_1	ν_{NH}	3529
ν_2	ν_{NCO} asymmetric	2269
ν_3	ν_{NCO} symmetric	1338
ν_4	δ_{HNC}	(776, not observed)
ν_5	δ_{NCO}	(577, not observed)
ν_6	δ_{NCO}	(656, not observed)

Table 3. HNCO storage capacity (µmol g^{-1}) and ν_{8a} values of coordinated pyridine.

Catalyst	[HNCO] (µmol g^{-1})*	LAS determined from pyridine FT-IR spectra			
		(µmol g)** RT	(µmol g)** 100°C	ν_{8a} (cm^{-1}) strong LAS	ν_{8a} (cm^{-1}) weak LAS
SiO_2	108	0.0	0.0	-	-
Al_2O_3	2200	114.9	78.6	1623	1615
ZrO_2	460	20.4	12.3	-	1605
TiO_2	275	17.3	11.4	-	1606
CeO_2	650	26.6	14.9	-	1599
Ce-Zr	1175	71.0	35.7	1607	1601
WO_3/Ce-Zr	754	51.1	43.9	1609	1603

* Determined from residual HNCO pressure at equilibrium (RT).

** Determined from pyridine evacuated at RT or 100°C.

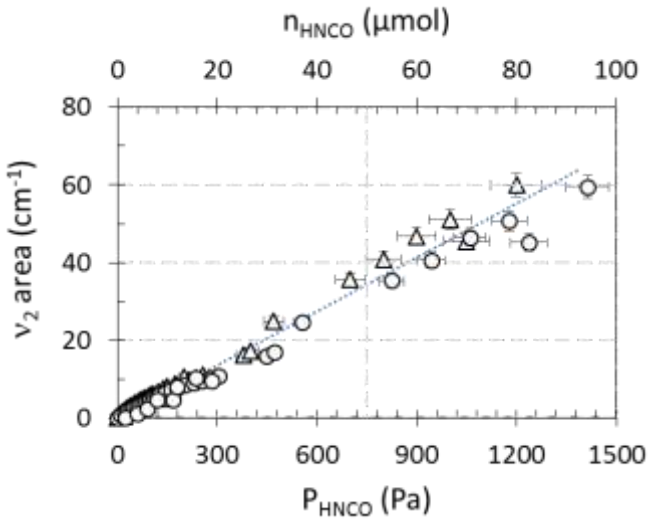

Figure 5. HNCO gaseous calibration for ν_2 mode. (○): n_{HNCO} (µmol); (△): P_{HNCO} (Pa).

3.4 HNCO ad-species over oxides-based samples

Spectra of adsorbed species over the studied oxide-based samples are presented in Fig. 6 after successive HNCO additions (up to 15 µmol) at RT. Among the studied oxides, SiO_2 was the only material that revealed no band of adsorbed species. Only the gas phase was observed (supplementary material, Fig. S3), in accordance with the previously recorded spectra of gaseous HNCO (Fig. 4).

On the contrary, exposure of Al_2O_3, ZrO_2, CeO_2, Ce-Zr and WO_3/Ce-Zr samples to controlled increments of HNCO up to 15 µmol caused the appearance of bands situated in the 2260-2150 cm^{-1} spectral region, assigned to isocyanate (–NCO) species adsorbed in various metal centres ($M^{\delta+}$–NCO) [xx-xxiii]. Then, HNCO adsorbs dissociatively on transition metal oxides, leading to isocyanate species bounded to Lewis acid sites (Eq. 4):

$$HNCO \rightarrow H_{(a)} + NCO_{(a)} \qquad (4)$$

Compared to ν_2 vibrational mode of gaseous HNCO (Fig. 3), the –NCO bands were redshifted, resulting in a reduction of the NCO force constant [xxiv]. No other compound was detected in the gas phase, as for instance CO which could be produced from Eq. 5. We may assume that N atoms formed from isocyanate decomposition recombined to yield N_2 (Eq. 6). However this process was not observed over transition oxide studied in this work. The dissociative adsorption of HNCO toward oxide-based samples is discussed thereafter. The observed shifts of adsorbed isocyanates species are compared to metal oxide properties in section 3.6.

$$NCO_{(a)} \rightarrow CO_{(g)} + N_{(a)} \qquad (5)$$

$$2\ N_{(a)} \rightarrow N_{2(g)} \qquad (6)$$

Al_2O_3. The interaction of –NCO species with alumina is probably the most reported in the literature, and bands at 2259 and 2233 cm^{-1} are attributed to $Al_{VI}NCO$ and to $Al_{IV}NCO$ species, respectively [xxv,xxvi]. These species were recorded from the first dose of HNCO addition and correspond to the highest wavenumbers observed over all the studied solids.

ZrO_2. In agreement with Knozinger *et al.* [xxvii], surface isocyanate species at 2231 cm^{-1} are observed over ZrO_2. With this solid, it seems that only one adsorption site was effective. The shift to the higher wavenumbers from 2225 cm^{-1} to 2231 cm^{-1} is assigned to the consequence of the building up of adsorbate-adsorbate interactions.

TiO_2. Over this material, the band at 2223 cm^{-1} can be attributed to isocyanates groups bounded to Ti^{4+} in accordance with previous works [xxviii,xxix]. As for ZrO_2, a shift was observed from 2195 to 2223 cm^{-1} together with the increase of the HNCO coverage.

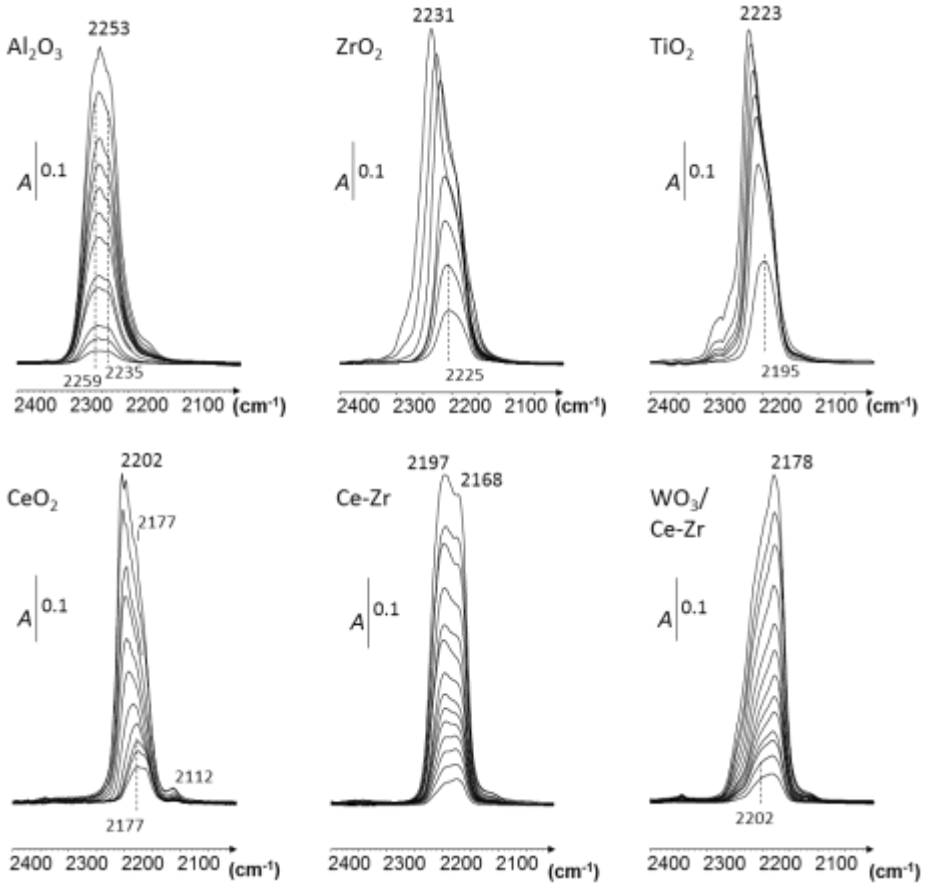

Figure 6. Addition of accurately known increments of HNCO up to 15 µmol (at RT) over oxide-based samples. Spectra are normalized to a disc of 10 mg cm^{-2}.

CeO_2. Exposure of CeO_2 to a very low pressure of HNCO firstly produced a band centered at 2177 cm^{-1}. The intensities increased with the rise of HNCO pressure, associated with a shift to higher wavenumbers, at 2202 cm^{-1}.Taking into account previous results obtained on ceria [xxx], both bands at 2202 and 2177 cm^{-1} are attributed to the asymmetric stretch of NCO species attached to CeO_2. The appearance of two bands suggests the presence of two adsorption sites, perhaps Ce^{4+} and Ce^{3+}. Additionally, the band at 2112 cm^{-1} is assigned to the $^2F_{5/2} \rightarrow {}^2F_{7/2}$ electronic transition band of Ce^{3+} [xxxi] that confirms the presence of both cationic sites (Ce^{4+}/Ce^{3+}).

CeO_2-ZrO_2. Exposure of CeO_2-ZrO_2 solid solution to HNCO led to the appearance of ν_{NCO} bands close to cerium oxide, with two adsorption sites. In fact, two bands were observed at 2197 cm^{-1} and 2168 cm^{-1} which grew simultaneously with the addition of HNCO. Based on these results and in accordance with the previous attribution over ZrO_2, we assigned these bands to the interaction of –NCO species with two cerium cation, as for ceria.

WO_3/CeO_2-ZrO_2. HNCO adsorption over WO_3/Ce-Zr firstly revealed a band at 2202 cm^{-1} which was quickly covered by the band at lower wavenumbers (2178 cm^{-1}). Compared to Ce-Zr host support, the

band related to –NCO species at lower wavenumbers (2178 cm^{-1}) presented higher intensity than the high wavenumbers component (2202 cm^{-1}). Additionally, the similar position of this band (2178 cm^{-1}) to that previously observed at the lowest wavenumbers for CeO_2 (2177 cm^{-1}) may indicate that WO_3 interfered preferentially with one cationic site of ceria support (Ce^{4+} or Ce^{3+}). However, this explanation would require further study.

3.5 Determination of the molar extinction coefficients ε_{NCO}

The intensities of the absorbance bands of the infrared spectra in the transmission mode depend on the amount of vibrating species through the optical path of the infrared beam. On homogeneous sample, IR absorbance can be used for quantitative analyses. The equation used is similar to the Beer-Lambert law for a solution. The absorbance integrated intensity for a band is named I, as reported by Eq. 7:

$$\mathrm{I} = \int_{\nu 1}^{\nu 2} A(\nu)\, \mathrm{d}\nu = \varepsilon\, \mathrm{d}(\mathrm{n}/\mathrm{Sd}) = \varepsilon \left(\frac{\mathrm{n}}{\mathrm{S}}\right) \qquad (7)$$

where $\mathrm{A}(\nu)$,ν, n, S and d denote the absorbance, the wavenumber, the number of vibrators, the area of the oxide disc and the thickness of the wafer assumed to correspond to the optical pathway [xxxii], respectively. From the addition of accurately known increments of HNCO previously reported in Fig. 6, the corresponding integrated intensities of ν_{NCO} band related to the isocyanate adsorbed species are plotted in Fig. 7 versus the amount of added HNCO (µmol cm^{-2}). The apparent molar extinction coefficient of the ν_2 mode of HNCO (ε_{NCO}) at RT is deduced from the obtained slopes as $\varepsilon = \mathrm{S}\ \frac{d(\mathrm{I})}{d\mathrm{n}}$ (ε in µmol^{-1} cm). Fig. 7 reveals some variations in the observed slope depending on the considered sample. However, the averaged extinction coefficient is 11.8 ± 1.8 cm µmol^{-1}.

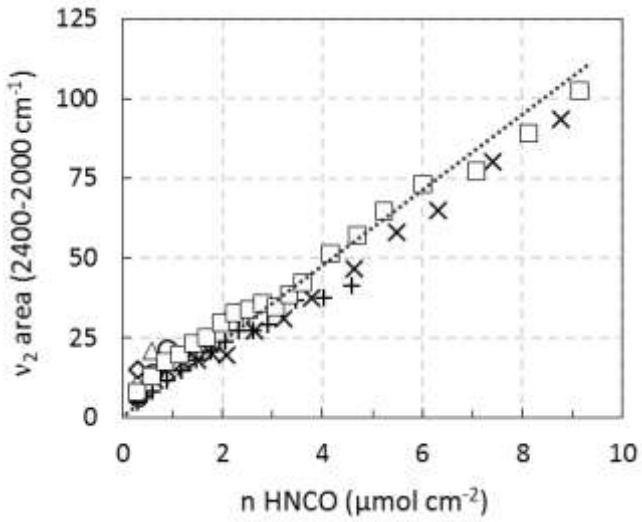

Figure 7. Integrated intensity of the ν_2 mode of HNCO versus addition of increments of HNCO (µmol cm^{-2}). (○): Al_2O_3; (□): WO_3/Ce-Zr; (×): CeO_2; (+): Ce-Zr; (◇): TiO_2; (△): ZrO_2.

Morterra *et al.* [xxxiii] presented a critical use of molar absorption coefficients for adsorbed species. They checked the validity of equations of the Beer–Lambert law for heterogeneous systems like silica for methanol adsorption. For instance, they reported that molar absorption coefficient values greatly vary depending on the silica provider. The suggested reasons were the catalyst specific surface area, the sample thickness, the surface dehydration level and the diffusion properties of the adsorbent. Consequently, the use of absorption coefficients in the Beer–Lambert law is not rigorous in the case of powder samples, since the absorption coefficients for adsorbed species depend on the optical properties of the solid, on the experimental conditions, and on the interaction between the solid and the adsorbed molecule. For instance, in our case, the studied samples presented very different specific surface area from 13 to 176 $m^2\ g^{-1}$ for TiO_2 and Al_2O_3, respectively. This important variation can explain the measured deviations from the calculation of the molar absorption coefficients.

In addition, it is well known that the molar extinction coefficients also depends on the adsorbing sites. The use of a global HNCO molar extinction coefficient regardless of multiple HNCO adsorption sites can lead to incorrect site quantification. As a consequence, the advanced values should be interpreted cautiously and the reported data have to be completed by coupling infrared spectroscopy and *in situ* thermogravimetry experiments for instance. Nevertheless, obtained extinction coefficients from HNCO adsorption appeared rather close together and the decomposition of cyanuric acid to yield pure gaseous isocyanic acid is a first step of deeper analytical works for *in situ* infrared studies of isocyanate species reactivity.

3.6 HNCO adsorption capacity, dissociative adsorption

In this section the maximum HNCO adsorption capacity of the various studied oxides was measured. The quantification of adsorbed species cannot be performed using the apparent molar coefficient due to the saturation of the detector for samples that displayed important HNCO adsorption abilities such as Al_2O_3, CeO_2, Ce-Zr and WO_3/Ce-Zr. Consequently, a more accurate estimation of the HNCO adsorption capacities resulted in the equilibrium pressure measurement between the relaxed amount in the cell and that obtained in the presence of the sample. From the previously calculated gas phase calibration (section 3.3, Fig. 5), the adsorbed amount can be determined.

Results reported in Table 3 illustrate the remarkable HNCO adsorption capacity of Al_2O_3 with around 2200 $\mu mol\ g^{-1}$. However, this oxide also exhibited higher specific surface area, with 176 $m^2\ g^{-1}$. Due to the important variation of the B.E.T values of the whole studied samples, the HNCO adsorption amount was correlated to the acid sites density ($\mu mol\ m^{-2}$), determined from pyridine adsorption (Fig. 3). It appears in Fig. 8A that the higher the LAS density, the higher the HNCO adsorption capacity. This result confirms that HNCO adsorption abilities was directly correlated to LAS, as previously proposed by

Solymosi *et al.* [xxi,xxii] (supplementary material, Fig. S4). Additionally, it is worth noting that acidic properties were determined from pyridine adsorbed under dynamic vacuum, whereas HNCO adsorption abilities were provided at equilibrium pressure. This explains the quantitative divergence of Fig. 8A. Nevertheless, catalysts behaviours are clearly distinguishable despite the experimental error, demonstrating the higher HNCO adsorption density for TiO_2 and ZrO_2 materials.

Finally, the higher wavenumbers of the ν_2 mode of adsorbed isocyanates (Fig. 6) is reported versus the ν_{8a} ring vibration of coordinated pyridine in Fig 8B. Both weak and strong LAS (Table 3) previously discussed in Fig. 2 are considered. It appears that HNCO dissociative adsorption mainly involves weak LAS location. Besides, due to the important wavenumbers variation of the $\nu_{as(NCO)}$ band depending on the studied material (2289-2177 cm^{-1}) together with the dissociative adsorption of HNCO, it appears that isocyanic acid could be an appropriate probe molecule for weak Lewis acid-base pairs.

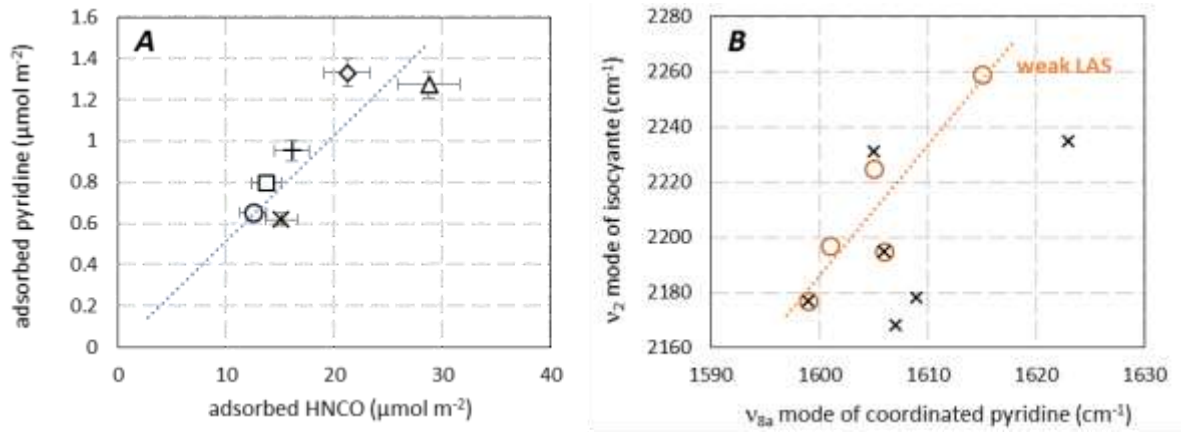

Figure 8. A: Relationship between LAS density determined from pyridine evacuated at RT and HNCO adsorption capacity. B: Relationship between the ν_2 mode of isocyanate and the ν_{8a} mode of coordinated pyridine (○: weak LAS; ×: strong LAS).
(○): Al_2O_3; (□): WO_3/Ce-Zr; (×): CeO_2; (+): Ce-Zr; (◇): TiO_2; (△): ZrO_2.

3.7 HNCO hydrolysis rate

HNCO hydrolysis is expected to produce ammonia in the NO_X SCR by urea process. To study the HNCO hydrolysis rate over the oxide-based samples, H_2O was added on the IR cell together with HNCO, as described in the experimental part. Both surface and gaseous IR spectra were recorded every 25°C from 25°C up to 400°C.

Examples of gaseous spectra are reported in Fig. 9A for alumina sample. Spectra are characterized by IR bands characteristic of HNCO ($\nu_{as(NCO)}$), CO_2 ($\nu_{as(OCO)}$), H_2O ($\delta_{(OH)}$) and NH_3 ($\delta_{(NH)}$) species. In this sample, HNCO seemed fully consumed at around 150 °C, concomitantly with NH_3 and CO_2 formation, whose maximum concentration was reached before 200°C. These results highlight the HNCO hydrolysis

reaction (Eq. 2). Besides, IR spectra of adsorbed species (supplementary material, Fig. S5) revealed that –NCO adsorbates were concomitantly consumed. This result suggests that hydrolysis of HNCO involves isocyanate species as intermediate. In fact, two mechanisms can be differentiated to highlight ammonia production, with the involvement or not of adsorbed intermediates. Unland [xxxiv] suggested that NH_3 is produced by HNCO hydrolysis, possibly via carbamic acid formation (Eq. 8). In this case, –NCO species are not suspected to be involved in the mechanism of NH_3 formation.

$$HNCO + H_2O \rightarrow (H_2NCOOH) \rightarrow NH_3 + CO_2 \quad (8)$$

$$NCO_{(a)} + H_2O \rightarrow NH_{2(a)} + CO_2 \quad (9)$$

$$NH_{2(a)} + H_2O \rightarrow OH_{(a)} + NH_3 \quad (10)$$

In this work, it is proposed that HNCO hydrolysis rather proceeds via a surface reaction of adsorbed isocyanate species, as illustrated by Eq. 9 and Eq. 10 resulting in the global following reaction (Eq. 11):

$$NCO_{(a)} + 2\ H_2O \rightarrow NH_3 + CO_2 + OH_{(a)} \quad (11)$$

The intensity of the NH_3 band can be monitored versus the temperature. Fig 9B shows that HNCO hydrolysis rate depended on the involved solid. All catalysts were fully selective in ammonia production. No other compounds than NH_3 and CO_2 were observed. HNCO was fully hydrolysed at 175-200 °C for all catalysts studied, but some oxides hydrolysed isocyanic acid already at 25 °C, such as CeO_2, WO_3/Ce-Zr and Ce-Zr which presented remarkable activities for HNCO hydrolysis. The following activity order was then obtained: WO_3/Ce-Zr = Ce-Zr > CeO_2 >> ZrO_2 > TiO_2 > Al_2O_3 >> SiO_2. Note that Kröcher *et al.* [xxxv] proposed the following ranking: ZrO_2 > TiO_2 > Al_2O_3 > H-ZSM-5 >> SiO_2, which is consistent with our results.

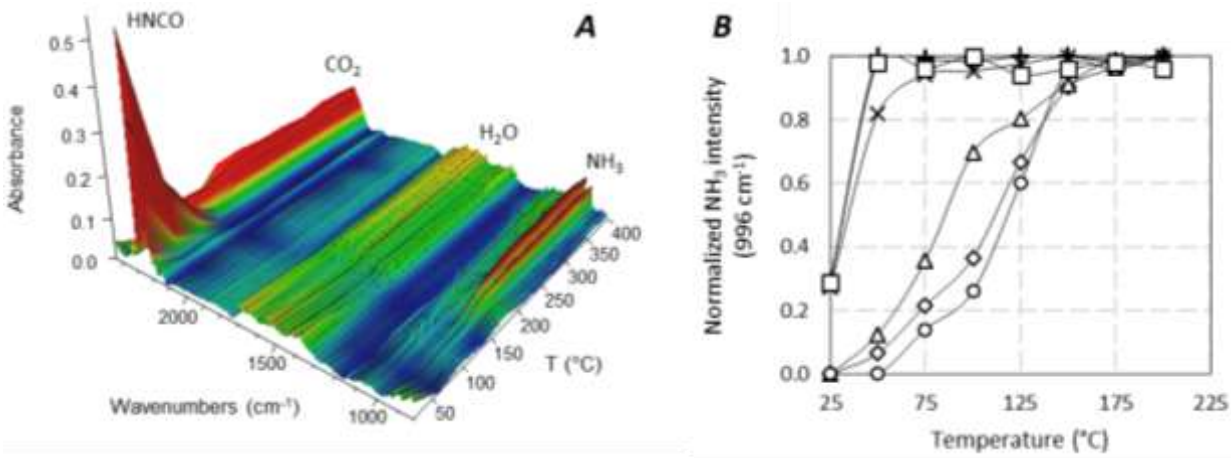

Figure 9. Gaseous IR spectra of HNCO hydrolysis reaction over Al_2O_3 from 25°C to 400°C (A); normalized evolution of the intensity of the NH_3 band at 966 cm^{-1} versus temperature for: (○): Al_2O_3; (□): WO_3/Ce-Zr; (×): CeO_2; (+): Ce-Zr; (◇): TiO_2; (△): ZrO_2.

4. Conclusion

Isocyanate species (–NCO) are well recognized as major intermediate in numerous deNO_x reactions, although few studies are openly devoted to their direct characterization. This work is a first step to a deeper knowledge of HNCO and adsorbed –NCO species reactivity by means of *in situ* FTIR spectroscopy. Pure gaseous isocyanic acid was obtained by depolymerising the cyclic trimer of cyanuric acid that allows HNCO adsorption monitored by FT-IR spectroscopy over a wide range of common oxides with various acid-base and redox properties: SiO_2, Al_2O_3, TiO_2, ZrO_2, CeO_2, CeO_2-ZrO_2, WO_3/CeO_2-ZrO_2. This study pointed out that HNCO adsorption is strongly dependent on transition metal adsorption sites, but also on the oxidation state of this latter. Molar extinction coefficients of adsorbed isocyanates species are proposed. They have to be used carefully, especially due to different specific surface area and multiple HNCO adsorption sites of the whole samples. Additionally, this work reveals the remarkable ability of TiO_2 and ZrO_2 solids to adsorb –NCO species. Co-adsorption of water illustrates the HNCO hydrolysis reaction rate, with an impressive reactivity of WO_3/Ce-Zr, Ce-Zr and CeO_2 materials to yield NH_3 and CO_2 at 25°C. For all oxide catalysts, -NCO species are reported as intermediate compounds of HNCO hydrolysis.

Acknowledgement

The authors thank the European communities (FEDER) and the “Région Nouvelle Aquitaine” for the financial support. Authors thank the “Engineering, development and technical support” division of the IC2MP laboratory for the implementation of the experimental analysis device: Michel Chauveau, Jean-Jacques Colin, Claude Veit, Claude Rouvier and Bertrand Leroux.

Supplementary Material

1. XRD characterisation

XRD patterns of the whole studied samples are presented in Fig. S1. Accordingly to the literature, alumina displays the classical γ-Al_2O_3 structure. TiO_2 mainly indicates rutile crystal phase (2θ = 27.4, 36.1 and 54.3°) with a low content (4%) of anatase mixture (2θ = 25.4, 37.9 and 48.1°). Pure CeO_2 sample is composed of cubic CeO_2 with fluorite structure at 2θ = 28.8, 47.7 and 56.5°. The addition of zirconia to ceria led to a shift of XRD peaks to higher values, and to the appearance characteristic peaks of monoclinic zirconia, at 2θ = 30.3, 50.5 and 44.8°. Consequently, the Ce-Zr (40-60) solid showed a broad band, observed at 2θ=29.1°, between pure c-CeO_2 (28.4°, JCPDS 34-0394) and pure t-ZrO_2 (30.2°, JCPDS 79-1766), which was attributed to $Ce_{0.5}Zr_{0.5}O_2$ solid solution due to the replacement of Ce^{4+} ions (0.97 Å) by the smaller Zr^{4+} ions (0.84 Å). After WO_3 impregnation over Ce-Zr, no modification of XRD patterns is observed, with no WO_3 XRD peaks detected, suggesting a good dispersion of tungsten trioxide phase.

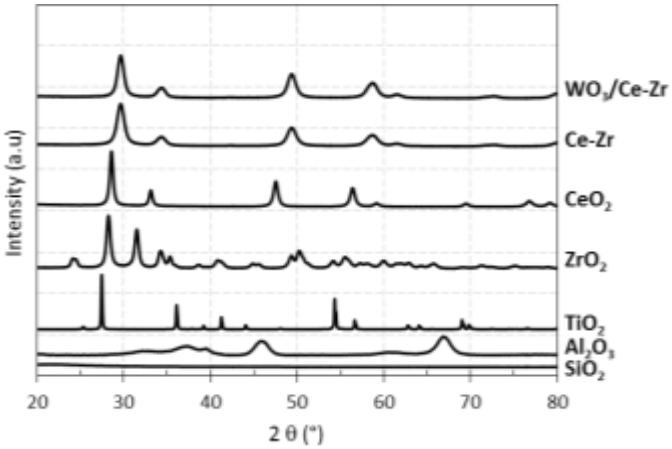

Figure S1. XRD patterns of oxides samples.

2. Surface acidity characterisation

Based on pyridine adsorption monitored by IR spectroscopy, the Lewis acid sites (LAS) concentration is calculated using the ν_{19b} mode of the ring vibration (ν_{CCN} stretch) of coordinated pyridine (1440-1455 cm^{-1}). The LAS concentration (expressed in µmol g^{-1}) of Al_2O_3, TiO_2, ZrO_2, CeO_2, Ce-Zr and WO_3/Ce-Zr samples is reported versus the pyridine temperature evacuation in Fig. S2.

It clearly appears that alumina present the higher LAS concentration of the whole studied catalysts. To the opposite, TiO_2, ZrO_2 and CeO_2 oxides are characterised by low Lewis acid sites concentration. The addition of ceria to zirconia enhance the acidic properties of the Ce-Zr sample compared to pure CeO_2 or ZrO_2 oxides. Additionally, the impregnation of WO_3 to Ce-Zr increases the strength of LAS with an improvement of coordinated pyridine concentration for high temperature evacuation compared to Ce-Zr host support.

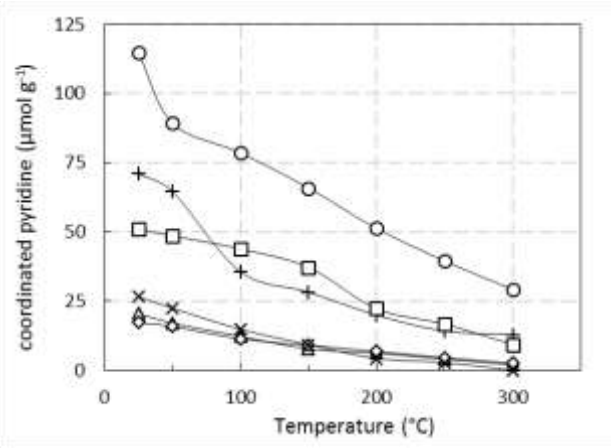

Figure S2. Lewis acid sites concentration (µmol g^{-1}) of the metal oxides. (○): Al_2O_3; (□): WO_3/Ce-Zr; (×): CeO_2; (+): Ce-Zr; (◇): TiO_2; (△): ZrO_2.

3. HNCO ad-species over SiO_2

Spectrum of adsorbed species after HNCO additions (10 µmol) at RT (spectra are normalised to a disc of 10 mg cm^{-2}) reveal that SiO_2 present no band of adsorbed species. Only the gas phase was observed as reported in Fig. S3. The band at 2269 cm^{-1} is assigned to the ν_2 mode of the asymmetric ν_{NCO} vibration of gaseous HNCO.

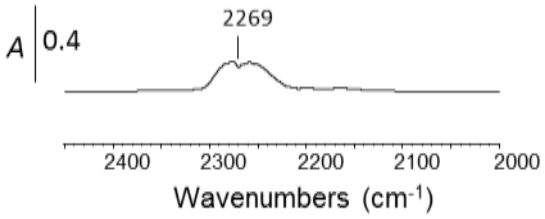

Figure S3. IR spectrum of HNCO adsorption (10 µmol) over SiO_2.

4. HNCO adsorption capacity

The HNCO adsorption capacity of the whole studied sample (Al_2O_3, TiO_2, ZrO_2, CeO_2, Ce-Zr and WO_3/Ce-Zr) was evaluated and compared to acidic sites concentration (µmol g^{-1}), determined from pyridine evacuation (Fig. S2). Results reported in Fig S4 indicate that higher the Lewis acid sites concentration, higher the HNCO adsorption capacity.

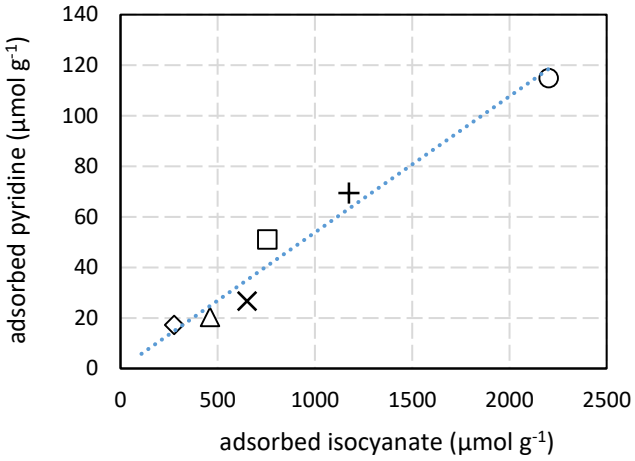

Figure S4. Relationship between LAS concentration determined from pyridine evacuated at RT and HNCO adsorption capacity (µmol g^{-1}). (○): Al_2O_3; (□): WO_3/Ce-Zr; (×): CeO_2; (+): Ce-Zr; (◇): TiO_2; (△): ZrO_2.

5. HNCO hydrolysis

The HNCO hydrolysis reaction is studied by expanding H_2O on the IR cell together with HNCO. Surface and gaseous IR spectra were successively recorded from 25 up to 400 °C by 25 °C step.

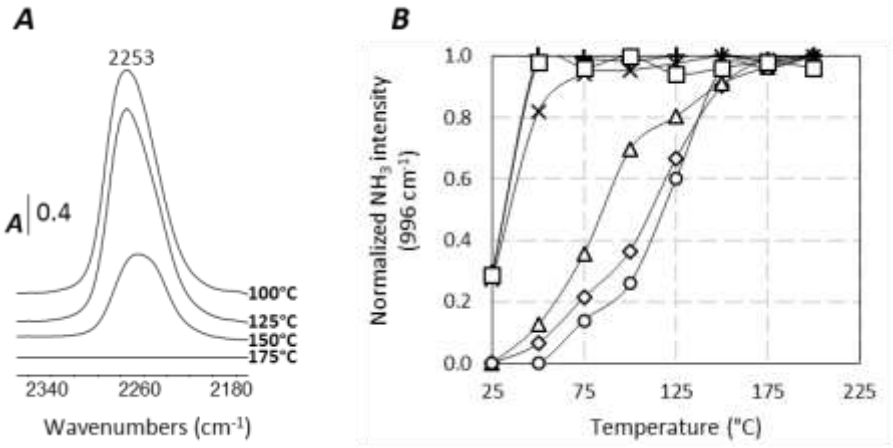

Figure S5. IR spectra of adsorbed species of HNCO hydrolysis over Al_2O_3 (A); normalized evolution of the intensity of the NH_3 band at 966 cm^{-1} versus temperature for: (○): Al_2O_3; (□): WO_3/Ce-Zr; (×): CeO_2; (+): Ce-Zr; (◇): TiO_2; (△): ZrO_2 (B).

IR surface spectra recorded over alumina sample are presented as example in Fig. S5A from 100°C to 175°C. The band at 2253 cm^{-1} is assigned to isocyanate (–NCO) species adsorbed on Al^{3+} metal centre. The intensity of –NCO band decrease with the increase in temperature to be fully consumed at temperature higher than 150°C. Concomitantly, gaseous NH_3 and CO_2 are observed in the gas phase, as the only reaction products. The intensity of the NH_3 band is reported Fig. S5B versus the temperature. It appears that –NCO compounds disappears together with gaseous ammonia production. This result suggests that hydrolysis of HNCO involves adsorbed isocyanate species as intermediate.

References

[i] W. Yang, R. Zhang, B. Chen, D. Duprez, S. Royer, Environ. Sci. Technol. 46 (2012) 11280−11288.
[ii] J. Liu, X. Li, Q. Zhao,C. Hao, D. Zhang, Environ. Sci. Technol. 47 (2013) 4528−4535.
[iii] F. Figueras, J.L. Flores, G. Delahay, A. Bourane, J.-M. Clacens, A. Desmartin-Chomel, B. Coq, A. Giroir-Fendler, Top. Catal. 39 (2006) 59-64.
[iv] F. Poignant, J. Saussey, J.C. Lavalley, G. Mabilon, J. Chem. Soc., Chem. Commun. (1995) 89-90.
[v] L. Capek, K. Novoveska, Z. Sobalık, B. Wichterlova, L. Cider, E. Jobson, Appl. Catal. B 60 (2005) 201–210.
[vi] A. Flura, X. Courtois, F. Can, S. Royer, D. Duprez, Top. Catal. 56 (2013) 94-103.
[vii] A.M. Bernhard, D. Peitz, M. Elsener, A. Wokaun, O. Kröcher, Appl. Catal. B., 115-116 (2012) 129-137.
[viii] M. Seneque, F. Can, D. Duprez, X. Courtois, ACS Catal., 6(7) (2016) 4064-4067.
[ix] R.A. Perry, D.L. Siebers, Nature, 1986, 324, 657-658.
[x] N. Apostolescu, B. Geiger, K. Hizbullah, M.T. Jan, S. Kureti, D. Reichert, F. Schott, W. Weisweiler, Appl. Catal., B., 62 (2006) 104-114.
[xi] G. Qi, R.T. Yang, R. Chang, Appl. Catal. B., 51 (2004) 93-106.
[xii] F. Can, S. Berland, S. Royer, X. Courtois, D. Duprez, ACS Catal., 3 (2013) 1120-1132.
[xiii] G. Larsen, E. Lotero, S. Raghavan, R.D. Parra, C.A. Querini, Appl. Catal. A., 139, 1996, 201-211.
[xiv] M. Tamura, K. Shimizu, A. Satsuma, Appl. Catal., 433 (2012) 135-145.
[xv] M.I. Zaki, M.A. Hasan, F.A. Al-Sagheer, L. Pasupulety, Colloids Surf A Physicochem Eng Asp., 190 (2001) 261-274.
[xvi] S. Triwahyono, T. Yamada, H. Hattori, H. Appl. Catal. A. 242 (2003) 101-109.
[xvii] A. Flura, F. Can, X. Courtois, S. Royer, D. Duprez, Appl. Catal. B., 126 (2012) 275-289.
[xviii] M.S. Lowenthal, R.K. Khanna, M.H. Moore, Spectrochim. Acta A., 58 (2002) 73-78.
[xix] J.H. Teles, G. Maier, B.A. Hess Jr, L.J. Schaad, M. Winnewisser, B.P. Winnewisser, Chem. Ber., 122 (1989) 753-766.
[xx] V.A. Matyshak and O.V. Krylov, Catal. Today, 25 (1995) 1-88.
[xxi] F. Solymosi and J. Raskó, J. Catal., 65 (1980) 235-237.
[xxii] F. Solymosi and T. Bánsági, J. Catal., 202 (2001) 205-206.
[xxiii] Y.H. Yeom, B. Wen, W.M.H. Sachtler, E. Weitz, J. Phys. Chem. B. 108 (2004) 5386-5404.
[xxiv] J. Ryczkowski, Catal Today, 68 (2001) 263-381.
[xxv] N. Bion, J. Saussey, M. Haneda, M. Daturi, J. Catal., 217 (2003) 47-58.
[xxvi] N. Bion, J. Saussey, C. Hedouin, T. Seguelong, M. Daturi, Phys. Chem. Chem. Phys., 3 (2001) 4811-4816.
[xxvii] T. Weingand, S. Kuba, K. Hadjiivanov, H. Knözinger, J. Catal., 209 (2002) 539-546.
[xxviii] F. Solymosi, T. Bansagi, J. Phys. Chem., 83(4) (1979) 552–553
[xxix] G. Halasi, T. Bánsági, F. Solymosi, J. Catal., 325 (2015) 60-67
[xxx] T. Bánsági, T.S Zakar, F. Solymosi, Appl. Catal. B., 66 (2006) 147-150.
[xxxi] C. Binet, A. Badri and J.C. Lavalley, J. Phys. Chem., 98 (1994) 6392-6398.
[xxxii] S. Khabtou, T. Chevreau, J.C. Lavalley, Microporous Mater., 3 (1994) 133-148.
[xxxiii] C. Morterra, G. Magnacca, V. Bolis, Catal Today, 70 (2001) 43-58.
[xxxiv] M.L. Unland, J. Phys. Chem., 77 (1973) 1952-1956.
[xxxv] A.M. Berhard, D. Peitz, M. Elsener, T. Schildhauer, O. Kröcher, Catal. Sc. Technol., 3 (2013) 942-951.